



Institute for

Shock Physics

WASHINGTON STATE UNIVERSITY

Direct observation of the hcp-bcc phase transition and melting along the principal Hugoniot of Mg

M. T. Beason, A. Mandal, B. J. Jensen

DOI: [10.1103/PhysRevB.101.024110](https://doi.org/10.1103/PhysRevB.101.024110)

Published Date: January 2020

Physical Review B

Direct observation of the hcp-bcc phase transition and melting along the principal Hugoniot of Mg

M. T. Beason, A. Mandal, B. J. Jensen

Shock and Detonation Physics (M-9), Los Alamos National Laboratory, Los Alamos, New Mexico 87545, USA

Time-resolved X-ray diffraction was used to examine the phase evolution of polycrystalline Mg shocked along the principal Hugoniot to states that span multiple phase boundaries into the liquid. The diffraction data indicate that the hcp-bcc phase boundary lies above 27 GPa, with the hcp-bcc transition occurring within nanoseconds of loading. Experiments at 55 GPa reveal a mixture of bcc and liquid, indicating incipient melt occurring 10-15 GPa lower than previously reported, with complete melting observed at 63 GPa.

Being the third period alkaline earth metal, Mg occupies an interesting place on the periodic table. It is the only element from the Alkali metals through the Cr group to not melt from the bcc phase at ambient conditions due, in part, to a shear instability in its bcc structure at low pressure [1]. Under ambient conditions, its electrons occupy s and p bands; however, at elevated pressure its behavior is governed by the occupancy of its previously empty 3d band [1,2]. This has led to Mg being the subject of a number of papers investigating computational methods for equations of state and phase transitions [1-8], and makes it a useful material for investigating experimental techniques at high pressure. The prediction of the hcp-bcc phase transition along the cold curve (0 K isotherm) prior to its observation along the room temperature isotherm was a major computational success [1,2,9]; however, extending this success to elevated temperatures has proven difficult.

Despite being a prototypical simple metal, the Mg phase diagram (Figure 1) is unsettled at finite temperature. The low-pressure hcp phase is found to coexist with bcc over a broad range of pressures and temperatures in static measurements [9,10]. Furthermore, the volume change along the Hugoniot is sufficiently small that it was only recently clear that the hcp-bcc transition even occurs under shock loading [11]. A dhcp phase has been observed at 5-20 GPa near the melt boundary [12]. The two studies that have investigated the melt boundary at pressures above 20 GPa agree up to 40 GPa but diverge above this pressure [10,13]. The discrepancies between experimental and computational results points to a lack of understanding of Mg at finite temperature, which could elucidate whether Mg plays a role in the density deficit of Earth's core [14-17] or shed light on how to stabilize bulk bcc-Mg at ambient conditions for use as a light structural material [18]. The location of the melt boundary and the temperature along the Hugoniot play critical roles in large scale hydrocode simulations that leverage state variables to determine material strength at high strain rates [19-22]. These codes often scale material strength based on the shear modulus and melting temperature to account for the loss of shear strength as the melt boundary is approached. As Mg is increasingly used as a light structural material accurate knowledge of its phase evolution under high-rate loading is becoming increasingly important.

In this work, we use dynamic XRD coupled with laser-driven shock wave experiments at the Advanced Photon Source (APS, Argonne, IL) to study the phase evolution of Mg along the principal Hugoniot (locus of thermomechanical states attained through single shock wave loading). While accurate temperature measurements during shock loading are still difficult, the internal energy, compression (Δ), and longitudinal stress (σ_x) are well defined by the Rankine-Hugoniot (R-H) jump conditions [23], and constitute some of the highest fidelity measurements at elevated temperature. Until recently the phase evolution along the Hugoniot could only be inferred from velocity profiles [23-27] guided by available static XRD data [10,12,13]. However, recent coupling of X-ray diffraction (XRD) techniques with dynamic loading platforms has enabled the phases formed during shock loading to be identified and the evolution of the microstructure to be examined on the nanosecond timescale [29-37]. Our results limit the region of possible hcp-bcc coexistence under shock loading and the stress at which Mg shock-melts on the principal Hugoniot. These measurements constrain the location of the phase boundaries and provide data essential for supporting theoretical EOS developments for Mg which have difficulty resolving the small energy differences in the hcp-bcc transition driven by s-d electron transfer at elevated temperatures [1-6].

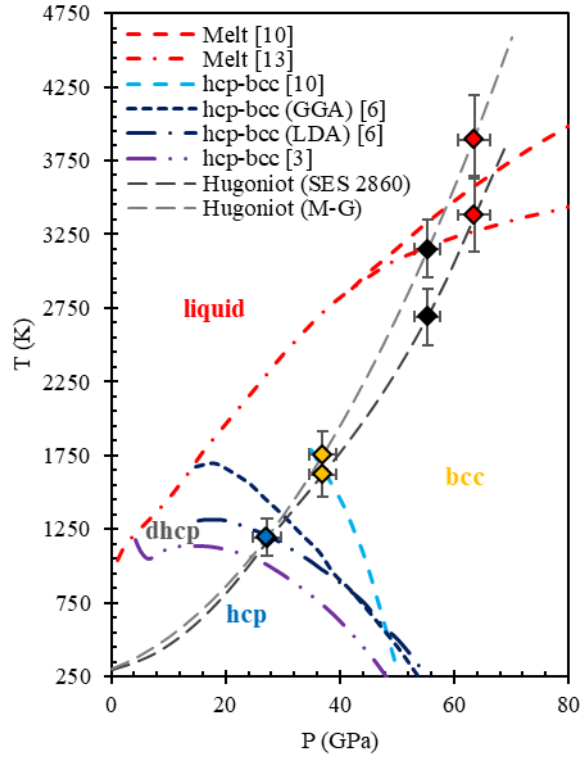


Figure 1 Phase diagram summarizing current theories on the location of the hcp-bcc phase boundary and the melt boundary as well as theoretical P-T Hugoniots for Mg, calculated using a Mie-Gruneisen or SESAME EOS (see text). The data points (diamonds) represent calculated temperatures at the experimentally observed shock stress for both P-T Hugoniots. Fill colors represent the phases identified through XRD except at 55 GPa, where liquid and bcc coexist.

Table I Experimental parameters and conditions. Symbols from left to right: Mg thickness (h), laser drive intensity (I), X-ray timing relative to shock breakout ($t_{x\text{-ray}}$), interfacial particle velocity (u_p^{int}), in material particle velocity (u_p^{Mg}), shock velocity (U_s), lateral stress (σ_x), density compression (Δ), and fraction of the sample at shock state (f_s).

Shot	h (μm)	I	$t_{x\text{-ray}}$ (ns)	u_p^{int} (mm/ μs)	u_p^{Mg} (mm/ μs)	U_s (mm/ μs)	σ_x (GPa)	Δ (%)	f_s
18-C-472	40 ± 3	30%	-0.93	1.7 ± 0.1	2.2 ± 0.1	7.2 ± 0.1	27 ± 2.5	29.9 ± 1.4	83%
18-C-473	30 ± 3	30%	-0.82	1.8 ± 0.1	2.2 ± 0.1	7.2 ± 0.1	27 ± 2.5	30.0 ± 1.4	80%
18-C-470	28 ± 3	40%	-1.10	2.2 ± 0.1	2.7 ± 0.1	7.9 ± 0.1	37 ± 2.7	34.1 ± 1.3	68%
18-C-471	29 ± 3	40%	-0.93	2.2 ± 0.1	2.7 ± 0.1	7.9 ± 0.1	37 ± 2.2	34.1 ± 1.3	75%
18-C-468	35 ± 3	50%	-0.70	2.9 ± 0.1	3.5 ± 0.1	8.9 ± 0.1	55 ± 2.2	39.3 ± 1.1	82%
18-C-467	33 ± 3	60%	-0.99	3.0 ± 0.1	3.6 ± 0.1	9.0 ± 0.1	56 ± 2.0	39.7 ± 1.1	73%
18-C-474	33 ± 3	60%	-1.4	3.0 ± 0.1	3.6 ± 0.1	9.0 ± 0.1	56 ± 2.0	39.7 ± 1.1	62%
18-C-469	32 ± 3	70%	-0.22	3.3 ± 0.1	3.9 ± 0.1	9.4 ± 0.1	64 ± 2.6	41.5 ± 1.1	93%
18-C-475	28 ± 3	70%	-0.12	3.2 ± 0.1	3.9 ± 0.1	9.4 ± 0.1	63 ± 2.6	41.2 ± 1.1	96%

Time-resolved XRD of laser shock loaded Mg was performed during hybrid mode operation at the Dynamic Compression Sector (DCS) of the APS. Details of the laser are given elsewhere [38]. As presented in Figure 2a, a 100 J, 351 nm laser with a 500 μm beam diameter was used to ablate Kapton mirrored with 30 nm of Al. The 10 ns laser pulse generated a shock wave that propagated through the remaining Kapton, and then into polycrystalline hcp-Mg foils (99.9% pure, Goodfellow USA) mounted on a 2 mm thick (100) LiF window. Sample thicknesses (h) are listed in Table I. The laser intensity (I) was varied from between 30-70% of the peak output. The X-rays were converted to visible light using a Gd₂O₂S:Tb phosphor scintillator, with subsequent images being captured by a CCD (Rayonix SX 165) with an 80 μm pixel size. The X-ray beam was approximately 40 μm in width and 20 μm tall with an energy maximum at 23.449 keV. The X-ray spectra used in this work is provided as supplemental material [39].

Point VISAR [40] was used to monitor the particle velocity at the Mg-LiF interface which provided both the peak stress state and its time duration. Representative wave profiles, presented in Figure 2b, show a shock jump to a peak state as the shock wave arrives at the Mg-LiF interface followed by a release wave that originated from the laser drive. A separate series of experiments (not shown here) using a Kapton-LiF target (no Mg sample) was used to characterize the laser drive. From these experiments and the VISAR data shown in Figure 2b) it was determined that the peak state was nominally 5 ns in duration prior to release and that the Mg samples were only partially shocked during the X-ray measurements with no evidence of a release state. The VISAR was operated in displacement mode, and therefore does not have a sub-nanosecond resolution. As a result, the apparent rise time associated with the shock is an artifact of the measurement technique, and not indicative of tilt in the incident wave.

A total of nine experiments were performed in this work with the relevant experimental parameters and measured or derived quantities presented in Table 1. Impedance matching using the R-H jump conditions coupled with the known shock response for Mg and LiF [41] were used to calculate the shock velocities (U_s) and in material Hugoniot states (particle velocity u_p^{Mg} , longitudinal stress σ_x , and density compression Δ) prior to the shock reflection from the LiF window. These results are presented in columns 6-9. Standard error propagation [42] was used to estimate the measurement uncertainties shown in the table.

Several corrections were applied to the diffraction images prior to radial integration [43]. Dark field images (no x-rays) and preshot background images (Kapton ablator only) were subtracted from the raw images. It was assumed that the background caused by the Kapton was independent of the peak stress because the ablator was in a released state during the X-ray measurements based on the VISAR data. The X-ray peaks from the unshocked LiF window were masked during integration with locations determined by the pre-shot image. Because the X-rays probed both shocked and unshocked regions of the Mg sample, the peaks corresponding to the unshocked state were removed by subtracting the ambient diffraction pattern scaled by the unshocked fraction ($1-f_s$), as determined using the h , U_s , and X-ray timing relative to motion at the sample/LiF interface ($t_{x\text{-ray}}$). The raw diffraction images for Mg and the Si reference are included in supplemental material [39].

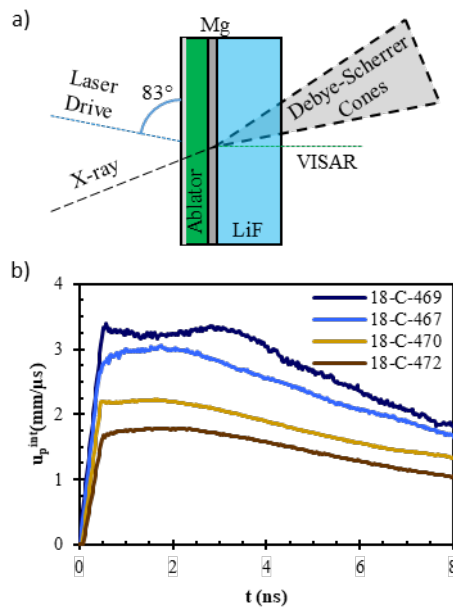


Figure 2 a) Experimental diagram showing the orientation of the laser drive and X-ray with respect to the target. b) Representative wave profiles from each pressure state.

The integrated XRD data, Figure 3, were analyzed to determine the peak positions and lattice compression for each experiment. Peak maxima were selected for each individual pattern and a least squares method was used to determine lattice parameters for a given structure assuming either an hcp ($P6_3/mmc$) or bcc ($Im-3m$) structure. The resulting peak locations are presented in Figure 3. At 27 GPa, hcp-Mg is still stable with a c/a ratio of 1.62, indicating a nearly ideal hcp structure. Increasing the σ_x to 37 GPa results in the formation of bcc-Mg; with three peaks being observable and explained by a bcc pattern. At 55 GPa a melt halo is observed, as highlighted by the gray dashed line. The peak coming out of the melt halo is attributable to the bcc (110), which is reasonably simulated using HiSPoD [44] sitting on a Gaussian contribution from the melt boundary. A slight peak observable at higher 2θ that could be the bcc (211). At 63 GPa, there

are no crystalline peaks present with the diffraction pattern being well fit by a single Gaussian contribution, indicating that the sample has completely melted.

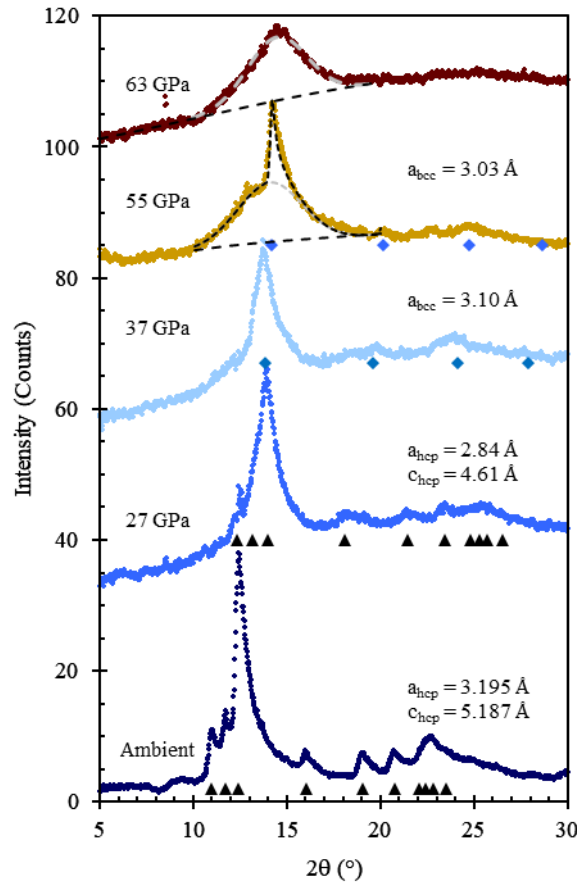


Figure 3 Measured diffraction patterns. The melt halo found in the 55 GPa and 63 GPa patterns are well fit by Gaussian profiles (dashed gray), with the 55 GPa pattern having an additional bcc contribution that has been simulated. Triangles and diamonds indicate indexed peak locations for hcp-Mg and bcc-Mg respectively.

Density compressions ($\Delta = 1 - \frac{\rho_0}{\rho} = 1 - \left(\frac{\sin \theta}{\sin \theta_0}\right)^{-3}$) at the peak state were estimated using both impedance matching [23] and the peak shift from the XRD data, Figure 4. The dashed line (gray) shows the Mg Hugoniot calculated using SESAME (SES) 2860 [45]. The close agreement between the impedance matching solution and the in situ compression shows directly that there is negligible tilt in the incident shock. Additionally, it provides confidence in the interpretation of the diffraction patterns presented in Figure 3, with the microstructural compression observed through diffraction matching the compression observed on the continuum level through velocimetry. The diffraction patterns show that polycrystalline Mg is compressed isotropically at the peak state and is well approximated in the hydrodynamic limit with the stress being equal to the pressure ($\sigma_x = \sigma_y = \sigma_z = P$).

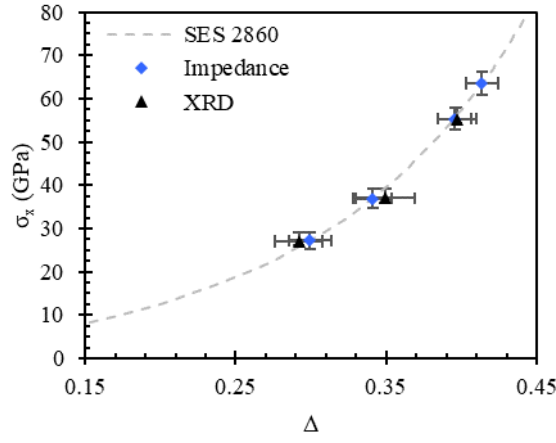


Figure 4 Comparison of measured and calculated density compressions.

For a Mie-Gruneisen (M-G) solid with $\gamma\rho = \gamma_R\rho_R$, constant heat capacity (C), and $U_s = C_0 + Su_p$, the temperature along the Hugoniot is given by

$$\begin{aligned}
 T^H(v) &= \exp\left(\frac{\gamma_r}{v_r}(v_r - v)\right) \left[T_0 \right. \\
 &\quad \left. - \frac{\rho_R^3 S C_0^2}{C} \int_{v_R}^v \exp\left(-\frac{\gamma_r}{v_r}(v_r - v')\right) \frac{(v_R - v')^2}{(1 - \rho_R S(v_r - v'))^3} dv' \right] \quad (1)
 \end{aligned}$$

where γ_R and ρ_R are the ambient Gruneisen parameter and density and T_0 is the initial temperature [46]. Taking $\gamma_R = 1.65$, Hugoniot parameters from Marsh et al. [40], and $C = 1.026 \frac{\text{kJ}}{\text{kg K}}$ [6] and assuming the hcp-bcc formation enthalpy is small (given the small volume change) gives the P-T Hugoniot presented in Figure 1. The assumption of a constant heat capacity is coarse; however, the heat capacity would typically be expected to increase with temperature. As such, inclusion of a non-constant heat capacity would act to reduce the reported temperature, making the M-G temperature a meaningful upper limit for the temperature along the Hugoniot barring any significant temperature increase across the hcp-bcc phase boundary. The P-T Hugoniot given by SES 2860 is also presented for comparison. These curves provide reasonable bounds for discussing our results within the Mg phase diagram.

There is currently some controversy over the boundaries of a dhcp phase observed in static experiments near the melt boundary [12]. It has been suggested that the Hugoniot intersects a region of dhcp stability near 20-35 GPa [47]. A dhcp diffraction pattern is very similar to an hcp diffraction with two key differences. In a dhcp pattern, the hcp (002) diffraction peak (the second peak in the hcp diffraction pattern) splits into the dhcp (101) and (004) peaks and an additional peak, the dhcp (103) peak, would be observed near 15.8° in the 27 GPa pattern. The diffraction results show no evidence of the dhcp phase at 27 GPa, making it unlikely that dhcp forms on the Hugoniot.

Our work agrees with Milathianaki et al. [11] with the hcp-bcc transition occurring on sub-nanosecond timescales; however, we clearly observe a compressed hcp phase at 27 ± 2.5 GPa with no evidence of bcc, while their results indicate the formation of bcc beginning at 26.2 ± 1.3 GPa with no mention of any mixed phase region. Our experiments were performed at a higher energy (23.5 keV compared to 4.7 keV) with increased intensity, which allowed the observation of several peaks (those above 20°) at d-spacings not probed by the previous work and may explain the difference. The diffraction pattern taken at 37 GPa falls where an hcp-bcc two phase region was observed in static experiments [10]. Our observation of a fully transformed bcc phase indicates that the hcp-bcc phase transition is complete at a lower P-T state than in static experiments, and limits any two-phase region to lie between 27 GPa and 37 GPa on the Hugoniot. The results from this work most closely agree with the boundaries taken from Mehta et al. [6], with the boundaries from Moriarty and Althoff [3] and Stinton et al. [10] under predicting and over predicting the transition stress along the Hugoniot respectively.

The diffraction data taken at 55 GPa and 63 GPa places clear limits on the melt boundary of Mg. The M-G and SES Hugoniots intersect the static melt boundary of Errandonea et al. [13] near 56 and 62 GPa respectively and that of Stinton et al. [10] at 58 GPa and 67 GPa respectively. Our results allow incipient melt to be conservatively estimated at 50-55 GPa with the temperature at 55 GPa being between 2550 K (SES) and 3120 K (M-G). This would estimate the melting point well below the 3200-3400

K at 55 GPa observed under static compression. In fact, the results show that the Hugoniot intersects the liquidus between 55 GPa and 63 GPa, below where incipient melt was expected based on the SES EOS. This indicates either a significant temperature increase occurring during the hcp-bcc transition or the melt boundary lying at lower temperatures than reported in static experiments. The former would be particularly surprising since there is not a measurable volume collapse observed along the Hugoniot, and would result in substantially lower strength than what current models would predict [19-22]. Furthermore, while undercooling in ramp solidification experiments is well documented [25, 28, 48], the completion of melting within a nanosecond at a stress-temperature state below the static melt boundary brings to question the role of superheating during shock driven melting of metals.

The XRD data for shocked Mg presented here provides clear limits on the locations of the hcp-bcc and melt phase boundaries along the principal Hugoniot as well as the rate at which these transitions occur. Our results show that both melting and the hcp-bcc transition occur on sub-nanosecond timescales and suggest that the hcp-bcc transition is likely martensitic. We find that the hcp-bcc phase boundary intersects the Hugoniot above 27 GPa, with Mg fully transforming to bcc by 37 GPa. Finally, at 55 GPa a mixture of bcc-Mg and liquid is observed form, indicating that the Hugoniot intersects the melt boundary at 50-55 GPa with melt completion prior to 63 GPa.

Acknowledgements

This work was supported by the US Department of Energy through the Los Alamos National Laboratory and performed at the Advanced Photon Source at Argonne National Laboratory. Joe Rivera, and John Wright are gratefully acknowledged for their help in target fabrication and assembly. Technical staff at Sector 35 including Adam Schumann, Nick Sinclair, Pinaki Das, Yuelin Li, Robert Zill, Drew Rickerson and Brendan Williams are thanked for their assistance with conducting the laser shock experiments. Los Alamos National Laboratory is operated by Triad National Security, LLC, for the national Nuclear Security Administration of the US Department of Energy (Contract No. 89233218CNA000001). Use of the Advanced Photon Source, an Office of Science User Facility operated for the DOE Office of Science by Argonne National Laboratory, was supported by the U.S. DOE under Contract No. DE-AC02-06CH11357. The Dynamic Compression Sector is supported by the Department of Energy (DOE), National Nuclear Security Administration, under Award Number DE-NA0002442 and operated by Washington State University (WSU).

-
- [1] J. D. Althoff, P. B. Allen, R. M. Wentzcovitch, and J. A. Moriarty, *Phys. Rev. B* 48, 13 253 (1993).
 - [2] J. A. Moriarty and A. K. McMahan, *Phys. Rev. Lett.* 48, 809 (1982).
 - [3] J. A. Moriarty and J. D. Althoff, *Phys. Rev. B* 51, 5609 (1995).
 - [4] R. M. Wentzcovitch and M. L. Cohen, *Phys. Rev. B* 37, 5571 (1988).
 - [5] F. Jona and P. M. Marcus, *J. Phys.: Condens. Matter* 15, 7727-7734 (2003).
 - [6] S. Mehta, G. D. Price, and D. Alfè, *J. Chem. Phys.* 125, 194507 (2006).
 - [7] C. J. Pickard and R. J. Needs, *Phys. Rev. Lett.* 102, 146401 (2009).
 - [8] P. Li, G. Gao, Y. Wang, and Y. Ma, *J. Phys. Chem. C* 114, 21745-21749 (2010).
 - [9] H. Olijnyk and W. B. Holzapfel, *Phys. Rev. B* 31, 4682 (1985).
 - [10] G. W. Stinton, S. R. Macleod, H. Cynn, D. Errandonea, W. J. Evans, J. E. Proctor, Y. Meng and M. I. McMahon, *Phys. Rev. B*, 90(13), 2014, pp. 134105.
 - [11] D. Milathianaki, D. C. Swift, J. Hawreliak, B. S. El-Dasher, J. M. McNaney, H. E. Lorenzana, and T. Ditmire, *Phys. Rev. B* 86, 014101 (2012).
 - [12] D. Errandonea, Y. Meng, D. H'ausermann, and T. Uchida, *J. Phys.: Condens. Matter* 15, 1277 (2003).
 - [13] D. Errandonea, R. Boehler, and M. Ross, *Phys. Rev. B* 65, 012108 (2001).
 - [14] N. Dubrovinskaia, L. Dubrovinsky, I. Kantor, W. A. Crichton, V. Dmitriev, V. Prakapenka, G. Shen, L. Vitos, R. Ahuja, B. Johansson, and I. A. Abrikosov, *Phys. Rev. Lett.* 95, 245502 (2005).
 - [15] K. Kádas, L. Vitos, B. Johansson, and R. Ahuja, *Proc. Natl. Acad. Sci. USA* 106, 15560 (2009).
 - [16] Y. Li, L. Vočadlo, D. Alfè, and J. Brodholt, *Phys. Earth Planet. Inter.* 274, 218-221 (2018).
 - [17] J. G. O'Rourke and D. J. Stevenson, *Nature* 529, 387-389 (2016).
 - [18] S. Pathak, N. Velisavljevic, J. K. Baldwin, M. Jain, S. Zheng, N. A. Mara, and I. J. Beyerlein, *Scientific reports* 7, 8364 (2017).
 - [19] G. R. Johnson and W. H. Cook, in *Proceedings of Seventh International Symposium on Ballistics*, The Hague, The Netherlands, April, 1983.
 - [20] F. J. Zerilli and R. W. Armstrong, *J. Appl. Phys.* 61, 1816 (1987).
 - [21] D. J. Steinberg, S. G. Cochran, and M. W. Guinan, *J. Appl. Phys.* 51, 1498 (1980).
 - [22] D. L. Preston, D. L. Tonks, and D. C. Wallace, *J. Appl. Phys.* 93, 211 (2003).
 - [23] J. W. Forbes, in *Shock compression of condensed matter: a primer* (Springer-Verlag, 2012).
 - [24] B. J. Jensen, G. T. Gray III, and R. S. Hixson, *J. Appl. Phys.* 105, 103502 (2009).
 - [25] D. H. Dolan, M. D. Knudson, C. A. Hall, and C. Deeney, *Nature Phys.* 3, 339 (2007).
 - [26] J. C. Boettger and D. Wallace, *Phys. Rev. B* 55, 2840 (1997).

- [27] J. H. Nguyen & N. C. Holmes, *Nature* 427(6972), 339 (2004).
- [28] P. C. Myint, A. A. Chernov, B. Sadigh, L. X. Benedict, B. M. Hall, S. Hamel, and J. L. Belof, *Phys. Rev. Lett.* 121(15), 155701 (2018).
- [29] M. G. Gorman, R. Briggs, E. E. McBride, A. Higginbotham, B. Arnold, J. H. Eggert, D. E. Fratanduono, E. Galtier, A. E. Lazicki, H. J. Lee, H. P. Liermann, B. Nagler, A. Rothkirch, R. F. Smith, D. C. Swift, G. W. Collins, J. S. Wark and M. I. McMahon, *Phys. Rev. Lett.* 115, 95701 (2015) doi: 10.1103/PhysRevLett.115.095701.
- [30] A. E. Gleason, C. A. Bolme, H. J. Lee, B. Nagler, E. Galtier, D. Milathianaki, J. Hawreliak, R. G. Kraus, J. H. Eggert, D. E. Fratanduono, G. W. Collins, R. Sandberg, W. Yang and W. L. Mao, *Nature Communications* 6, 8191 (2015) doi: 10.1038/ncomms9191.
- [31] P. Kalita, P. Specht, S. Root, N. Sinclair, A. Schuman, M. White, A.L. Cornelius, J. Smith, S. Sinogeikin, *Phys. Rev. Lett.* 119(25): 255701 (2017).
- [32] S. J. Turneure, S. M. Sharma, and Y. M. Gupta, *Phys. Rev. Lett.* 121(13): 135701 (2018)
- [33] S. J. Tracy, S. J. Turneure, T. S. Duffy, *Phys. Rev. Lett.* 120(13): 135702 (2018).
- [34] M. G. Newman, R. G. Kraus, M. C. Akin, J. V. Bernier, A. M. Dillman, M. A. Homel, S. Lee, J. Lind, J. L. Mosenfelder, D. C. Pagan, N. W. Sinclair and P. D. Asimow, *Geophys. Res. Lett.* 45(16): 8129-8135 (2018).
- [35] P. Renganathan, S. J. Turneure, S. M. Sharma, and Y. M. Gupta *Phys. Rev. B* 99(13): 134101 (2019).
- [36] R. Briggs, F. Coppari, M. G. Gorman, S. J. Tracy, A. L. Coleman, A. Fernandez-Pañella, M. Millot, J. H. Eggert, and D. E. Fratanduono, *Phys. Rev. Lett.* 123, 045701 (2019).
- [37] S. M. Sharma, S. J. Turneure, J. M. Winey, Y. Li, P. Rigg, A. Schuman, N. Sinclair, Y. Toyoda, X. Wang, N. Weir, J. Zhang, and Y. M. Gupta, *Phys. Rev. Lett.* 123, 045702 (2019).
- [38] X. Wang, P. Rigg, J. Sethian, N. Sinclair, N. Weir, B. Williams, J. Zhang, J. A. Hawreliak, Y. Toyoda, Y. M. Gupta, Y. Li, D. Broege, J. Bromage, R. Earley, D. Guy, and J. Zuegel, *Rev. Sci. Instrum.* 90, 053901 (2019).
- [39] See Supplemental Material at [URL will be inserted by publisher] for the raw diffraction images, X-ray energy spectrum, and representative laser pulse waveform.
- [40] D. H. Dolan, *Foundations of VISAR analysis*, Report: SAND2006-1950, (2006).
- [41] S. P. Marsh, *LASL Shock Hugoniot Data* (University of California Press, Berkeley, CA, 1980).
- [42] J. R. Taylor, *Introduction to error analysis, the study of uncertainties in physical measurements* (University Science Books, 1997).
- [43] B. H. Toby, R. B. Von Dreele, *Jour. Appl. Crystall.* 46(2):544-9 (2013).
- [44] T. Sun and K. Fezzaa, *J. Synchrotron Radiat.* 23, 1046(2016).
- [45] J. D. Johnson and S. P. Lyon, Los Alamos National Laboratory Technical Report No. LA-UR-92-3407, 1992 (unpublished).
- [46] L. Davison, in *Fundamentals of shock wave propagation in solids* (Springer-Verlag, 2008). [47] G. V. Sinko and N. A. Smirnov, *Phys. Rev. B* 80, 104113 (2009).
- [48] A. E. Gleason, C. A. Bolme, E. Galtier, H. J. Lee, E. Granados, D. H. Dolan, C. T. Seagle, T. Ao, S. Ali, A. Lazicki, D. Swift, P. Celliers, and W. L. Mao, *Phys. Rev. Lett.* 119, 025701 (2017).